BNL–111801–2016–JA

Use of High-granularity CdZnTe Pixelated Detectors to Correct Response Non-uniformities Caused by Defects in Crystals

A. E. Bolotnikov[a,*], G. S. Camarda[a], Y. Cui[a], G. De Geronimo[a], J. Eger[b], A. Emerick[b], J. Fried[a], A. Hossain[a], U. Roy[a], C. Salwen[a], S. Soldner[b], E. Vernon[a], G. Yang[a], and R. B. James[a]

[a]*Brookhaven National Laboratory, Upton, NY 11793, USA*
[b]*eV Products Inc., Saxonburg, Pennsylvania, 16056, USA*

Submitted to the Nuclear Instrument & Methods in Physics Research Section A – Accelerators Spectrometers Detectors and Associated Equipment

January 2016

Nonproliferation and National Security Department
Radiation Detector and Nonproliferation R&D
Brookhaven National Laboratory

U.S. Department of Energy

USDOE National Nuclear Security Administration (NNSA),
Office of Nonproliferation and Verification Research and Development (NA-22)

Notice: This manuscript has been authored by employees of Brookhaven Science Associates, LLC under Contract No. DE– SC0012704 with the U.S. Department of Energy. The publisher by accepting the manuscript for publication acknowledges that the United States Government retains a non–exclusive, paid–up, irrevocable, world–wide license to publish or reproduce the published form of this manuscript, or allow others to do so, for United States Government purposes.

[*]A. Bolotnikov. Tel.: +1-631-344-8014; fax: +1-631-344-5266; e-mail: bolotnik@bnl.gov.

DISCLAIMER

This report was prepared as an account of work sponsored by an agency of the United States Government. Neither the United States Government nor any agency thereof, nor any of their employees, nor any of their contractors, subcontractors, or their employees, makes any warranty, express or implied, or assumes any legal liability or responsibility for the accuracy, completeness, or any third party's use or the results of such use of any information, apparatus, product, or process disclosed, or represents that its use would not infringe privately owned rights. Reference herein to any specific commercial product, process, or service by trade name, trademark, manufacturer, or otherwise, does not necessarily constitute or imply its endorsement, recommendation, or favoring by the United States Government or any agency thereof or its contractors or subcontractors. The views and opinions of authors expressed herein do not necessarily state or reflect those of the United States Government or any agency thereof.

Use of High-granularity CdZnTe Pixelated Detectors to Correct Response Non-uniformities Caused by Defects in Crystals

.

A. E. Bolotnikov[a,*], G. S. Camarda[a], Y. Cui[a], G. De Geronimo[a], J. Eger[b], A. Emerick[b], J. Fried[a], A. Hossain[a], U. Roy[a], C. Salwen[a], S. Soldner[b], E. Vernon[a], G. Yang[a], and R. B. James[a]

[a]*Brookhaven National Laboratory, Upton, NY 11793, USA*

[b]*eV Products Inc., Saxonburg, Pennsylvania, 16056, USA*

Abstract

Following our successful demonstration of the position-sensitive virtual Frisch-grid detectors, we investigated the feasibility of using high-granularity position sensing to correct response non-uniformities caused by the crystal defects in CdZnTe (CZT) pixelated detectors. The development of high-granularity detectors able to correct response non-uniformities on a scale comparable to the size of electron clouds opens the opportunity of using unselected off-the-shelf CZT material, whilst still assuring high spectral resolution for the majority of the detectors fabricated from an ingot. Here, we present the results from testing 3D position-sensitive 15x15x10 mm^3 pixelated detectors, fabricated with conventional pixel patterns with progressively smaller pixel sizes: 1.4, 0.8, and 0.5 mm. We employed the readout system based on the H3D front-end multi-channel ASIC developed by BNL's

[*]A. Bolotnikov. Tel.: +1-631-344-8014; fax: +1-631-344-5266; e-mail: bolotnik@bnl.gov.

Instrumentation Division in collaboration with the University of Michigan. We use the sharing of electron clouds among several adjacent pixels to measure locations of interaction points with sub-pixel resolution. By using the detectors with small-pixel sizes and a high probability of the charge-sharing events, we were able to improve their spectral resolutions in comparison to the baseline levels, measured for the 1.4-mm pixel size detectors with small fractions of charge-sharing events. These results demonstrate that further enhancement of the performance of CZT pixelated detectors and reduction of costs are possible by using high spatial-resolution position information of interaction points to correct the small-scale response non-uniformities caused by crystal defects present in most devices.

Keywords: CdZnTe, high-granularity detectors, 3D pixelated detectors, crystal defects, charge sharing, charge-loss correction

---

1. Introduction

3D position-sensitive CdZnTe (CZT) pixelated detectors, developed by the team from the University of Michigan, offer significant enhancements in CZT detector spectral performance and the capability for gamma-ray imaging [1-4]. Further improvements of their position resolution will allow for more accurate corrections of detector-response non-uniformities, which will further increase the spectral and spatial resolution of CZT detectors and increase their acceptance for practical applications. Rrecently, we demonstrated the feasibility of correcting the small-scale response inhomogeneity and enhancing the performance of position-sensitive virtual Frisch-grid CZT detectors fabricated from unselected off-the-shelf CZT crystals [5]. By reading the signals from 4 strips placed on the device's side surfaces and using this information to measure the coordinates of the interaction points with an accuracy of ~100 μm, we achieved high-granularity segmentation of these detectors, up to 60x60x150 voxels. The measured signals generated in each of these voxels by interaction events were corrected before adding the events to the pulse-height spectrum. The three-dimensional response matrix, used to apply the in-fly corrections, was

obtained by calibrating each of the voxels before measurements. As a result, we improved the energy resolution of different 6x6x15 mm^3 detectors from 1.5-2.5% to 0.6-1.1% FWHM at 662 keV.

The goal of the work presented here was to demonstrate that high-granularity position sensing could also be applied to enhance the performance of large-volume pixelated detectors fabricated from unselected off-the-shelf CZT crystals.

Signals measured in CZT detectors are always affected by carrier trapping in crystals. In high mu-tau product material, $>10^{-2}$ V/cm^2, the trapping centers have low concentrations and should not be a problem provided their spatial distributions are uniform inside the crystals. Unfortunately, the dislocations and subgrain boundaries, commonly present in commercial CZT material, cause non-uniformities in the trapping centers distributions and, thus, fluctuations of the collected-charge signals. We note that variations of the collected-charge signals are solely attributed to random distributions of the interaction points and therefore can be corrected by making high-granularity detectors.

Two approaches can be considered to enhance the spatial resolution in pixelated detectors by using the collected- and transient-charge signals. The first approach [8-10] is applied when the whole charge from the electron cloud is collected on a single pixel. In such cases, the electron cloud induces transient signals on neighboring pixels, and the X-Y coordinates of interaction points can be obtained from the amplitudes of the transient signals. Theoretically, this approach should provide a sub-pixel resolution, but only within a geometrical area limited by the size of the electron cloud. The second approach is applied when the total charge from the electron cloud is shared between two or more neighboring pixels. As in the previous approach, the signal amplitudes corresponding to these pixels can be used to refine the positions of the interaction points with accuracy better than the pixel size, but, as in the previous case, within a certain geometrical area limited by the size of the electron cloud. In reality, both types of events occur in pixelated detectors with the relative number of shared events increasing with a decreasing pixel size. The total charge from the electron cloud can be collected on a single pixel (single-pixel events), or it can be shared among several pixels (charge-sharing events). This means that both approaches should be combined to evaluate the coordinates of the interaction points in pixelated detectors. Recently, Montemont *et al*. [11] demonstrated a novel algorithm for processing waveforms captured after charge-sensitive preamplifiers to refine the positions of the interaction points. Its key feature is that it uses time-correlated (synchronized) sampling amplitudes from several

pixels, regardless of whether the signals generated on the pixels are collecting or transient. We will discuss this approach in detail in Section 2.3.

For this study, we employed pixelated detectors with conventional contact patterns similar to the ones used in 3D devices, but with smaller dimensions, and relied on charge sharing for attaining high-granularity position resolution. We undertook three runs of measurements using pixelated detectors fabricated with progressively smaller pixel sizes from the same set of CZT crystals used for each consecutive run of measurements. For the performance baseline, we measured the pulse-height spectra from the 1.4-mm pixel size detectors, for which most of the electron clouds generated by the interaction events are collected on a single pixel. In contrast, for 0.8- and 0.5-mm pixel detectors, the majority of the events are shared between several adjacent pixels, allowing the high-granularity segmentation to improve the overall performance of these detectors.

2. Experimental

We conducted three runs of measurements to evaluate the performance of twelve 15x15x10 mm^3 3D position-sensitive pixelated detectors fabricated from the same set of CZT crystals, but with progressively smaller pixel sizes, viz., 1.4, 0.8, and 0.5 mm. To read the signals generated in the detectors, we employed the data-acquisition system based on the H3D front-end ASIC developed in collaboration between BNL's Instrumentation Division and the University of Michigan [12-15]. By using the same crystals to fabricate the detectors for each next run, we were able to directly assess the effect of a reduction in pixel size (or higher granularity) on device performance.

Since the goal of this work was to demonstrate the feasibility of using high-granularity position sensing to correct the response non-uniformities in pixelated detectors, we were not concerned with reconstructing the multiple interaction point events caused by the Compton scatterings. Instead, for the analysis, we selected only single-point interaction events, which we used to plot the pulse-height spectra and evaluate the width of their photopeaks. We note that single-point interaction events still can be collected on several adjacent pixels. We set a limit of 4 on the maximum number of pixels per event; the events with a greater number of hit pixels would be an indication of multiple point interactions as will be explained in Section 2.3.

As mentioned in the Introduction, for the performance baseline we used detectors with a 1.4-mm pixel pitch. In these detectors, the majority of interactions produced single-pixel events, for which we applied the drift-time

corrections (along Z-coordinate) only. Therefore, we anticipated that the energy resolutions of 1.4-mm pixel size detectors would be affected by small-scale non-uniformities. By comparing the energy resolution measured for the baseline detectors with those measured in the second and third runs, we could demonstrate the advantages of high-granularity pixelated detectors.

2.1. Detectors and front-end ASIC

Four 15x15x10 mm^3 CZT crystals, grown by the High-Pressure Electro-Dynamic-Gradient technique [16], were acquired from eV Products Inc. The crystals were cut from spectroscopy-grade material with a resistivity of $>3x10^{10}$ Ohm-cm and a mu-tau product of $>7x10^{-3}$ cm^2/V. Before fabricating the actual devices, we screened the crystals to reveal the presence and extent of extended defects, which are present inside the material, using white X-ray diffraction topography (WXDT) at BNL's National Synchrotron Light Source (NSLS).

Detectors with conventional contact patterns, comprising 11x11 square pixels (a 10x10 pattern was used for the first run) and 25-μm gaps between the pixel contacts, were fabricated by eV Products and mounted on the ceramic fanout boards using the reworkable conductive-epoxy bonding technology that allowed us to reuse the same crystals in the subsequent rounds of measurements. There was no interposing grid between the pixel contacts. For measuring the performance baseline (first run), we used detectors with a 1.4-mm pitch. For the second- and third-runs we used, correspondingly, 0.8- and 0.5-mm pixel pitches.

The readout system with the communication interface and low-voltage converters was enclosed inside a light-tight aluminum box that had a thin entrance window for the gamma rays. Fig. 1 shows the design of the 10x10 contact pattern, (a) the assembled detector mounted on the fanout substrate, and (b) the test box with a detector plugged into the motherboard (c). During the measurements the test box was placed inside an environmental chamber, where heat generated by the ASIC was drawn out, maintaining the temperature of the detector at around 18 degrees Centigrade. An uncollimated ^{137}Cs source with an activity of ~10 μCi was placed ~1 cm above the detector's cathode. Each measurement run usually took 2-3 days, the time needed to accumulate several gigabyte-size files containing a continuous data stream of the captured signal amplitudes and timing. For these measurements, we used the following ASIC settings: 1-μs peaking time for the anodes and the cathode's energy, and 0.2 μs for the cathode's timing. The cathode's bias was set at 2000 V.

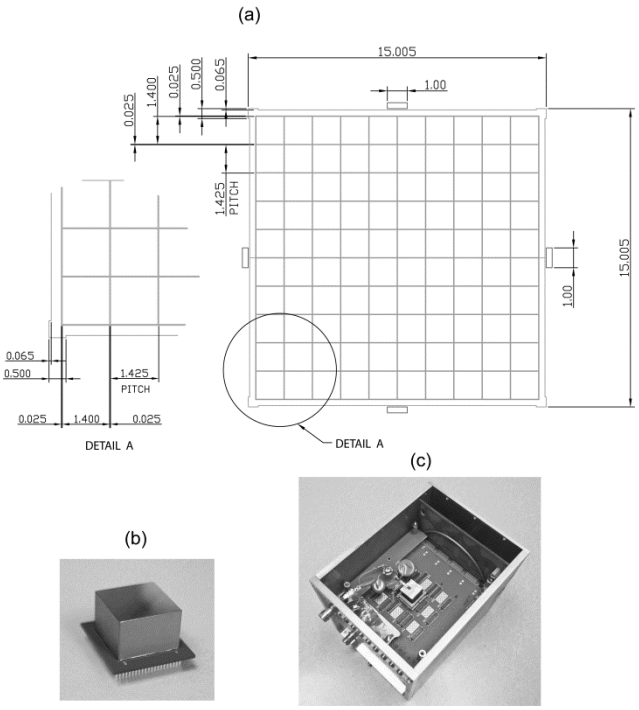

Fig. 1. 15x15x10 mm^3 pixelated CZT detectors used in these measurements: (a) The layout of the conventional anode pattern (dimensions in mm); (b) a detector mounted on the ceramic fanout; and, (c) the test box with a single detector plugged into the motherboard. We note that pixel pattern has no interposing grid.

Strong diffusion and electrostatic repulsion of the electrons in CZT cause significant broadening of electron clouds before they reach the anodes. This is particularly important in pixelated detectors with their higher probability of charge-sharing events, which can degrade the device's performance. One problem associated with such events is the charge loss in the gaps between the pixel contacts. Because of the high conductivity of a CZT surface, the electric field lines are virtually perpendicular to the crystal's surface between the contacts, meaning that a small fraction of the electron cloud will be trapped in the gaps between the contacts. However, the trapped carriers still induce signals on the adjacent pixels, whose amplitudes are dependent on the pixel sizes, gaps between the contacts, and the distance between the crystal's surface and the fanout substrate or any other shielding electrode. If the inter-pixel gaps are small compared to the gap between the anode's surface and the ground plane, then full signals will be generated on the adjacent pixels, as if the pixel contacts actually collected all the carriers. In such cases, no interposing grids are needed [17].

The second problem is related to the processing of the captured signals to determine the amount of charge actually collected on the pixel contacts. Whenever charge sharing takes place, both the collected- and the induced-charge (transient) signals are generated on the neighboring pixels. In the cases of conventional analog processing, when both components are integrated by the shaping amplifier, the transient signals can alter the measured collected charge, as if they were affected by the charge loss in the gaps between the pixels. The magnitude of this effect depends on the geometry; detectors with small pixels are less susceptible to this effect than those with large ones. An alternative and preferred approach would be the direct processing of digitized signals after the charge-sensitive preamplifiers, which provides undistorted information for handling charge-sharing events and correcting non-uniformities in the response.

The H3D ASIC used in this work is the most advanced readout-chip of its class developed for reading signals from large-volume 3D position-sensitive pixelated detectors. However, its major limitation, which is particularly critical when it is used for reading signals from detectors with large fractions of charge-sharing events, is its conventional (analog) signal processing. We discuss the implications of this later in this section.

The H3D ASIC [12-15] provides information on the amplitude and timing of each event captured from 121 anode and 2 cathode channels after shapers. Since the signals from the anodes and cathode have opposite polarities and different rise times, they have to be processed differently. Each anode channel includes a low-noise charge-sensitive amplifier, a baseline stabilizer, and a fifth-order unipolar shaping amplifier with an adjustable peaking time. Similarly, the cathode channel implements a charge-sensitive amplifier optimized for a cathode-input capacitance; however, it is followed by two parallel filtering- and processing-circuitries, one with a long shaping time for measuring the amplitude, and the other for measuring the timing. The beginning of the slow-rising slope of the cathode signal after the charge-sensitive preamplifier indicates the occurrence time of the interaction event, while the moment when the fast-rising anode (signal after the charge-sensitive preamplifier) reaches its maximum corresponds to the arrival of the electron cloud at the anode. ASIC identifies these time using the analog pulse processing. There are 4 optional methods implemented in the ASIC to determine the beginning of the slow-rising slope of the cathode signal [13]. In this work, we used the one based on the fast bipolar shaping (see Ref. [13] for details). The timing resolution of the ASIC is ~20 ns.

In the acquisition state, the ASIC waits for the above-threshold signal in any of the anode channels. Once this happens the ASIC starts capturing the peaks and times from the pixels of interest, even though some signals could be below the threshold, i.e. noise. The anode times are assigned corresponding to the peaks of the captured signals, making the measurements to the first order independent of the signal amplitudes [13]. The first channel, whose signal goes above the threshold, triggers the interaction event. The acquisition-stop signal (common to all channels) is generated in response to the trigger after a certain delay set by the user. It serves as a time reference for the timing measurements in all channels.

After the acquisition is complete, the peaks and corresponding amplitudes of timing are measured for all above-threshold anodes, including the surrounding ones, and routed to the output data-stream. Using time- and energy-calibration tables, the peak amplitudes then are converted into collected charges, while the differences between the amplitudes of the cathode's and the anode's timing ramp give the electron clouds' drift times.

2.2. Signals generated in pixelated detectors

There are two kinds of signals generated on the anode contacts in pixelated detectors: collected- and induced-charge signals. They co-exist in the case of charge-sharing events, which constitute a major problem for signal processing in pixelated detectors, especially for detectors with an analog ASIC readout. The induced signals are also called transients, because they are generated by the movement of carriers that are collected eventfully on other pixels. Fig. 2 illustrates the charge signals (waveforms) measured after the charge-sensitive preamplifiers from three adjacent pixels, corresponding to a double-pixel event when only two pixels share the electron cloud: pixels 1 and 2 in this case. The signal captured from the pixel 3 is a pure induced (transient) signal. These waveforms were measured with our previously tested detector with a pixel size of 2 mm.

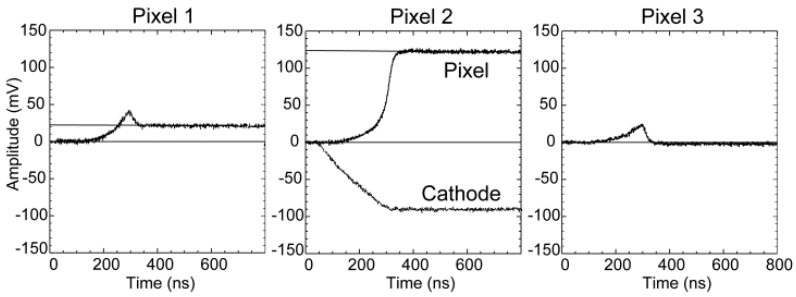

Fig. 2. The waveforms captured after charge-sensitive preamplifiers from the cathode and three adjacent pixels, showing the differences in the shapes of collected- and induced-charge signals. The solid lines represent the signal levels corresponding to the amounts of the collected charge.

Because of charge sharing, the waveform measured from pixels 1 and 2 can be considered as a superposition of the collected- and the induced-charge signals generated, respectively, by the collected and transient carriers. In the example shown in Fig. 2, the majority of the charge was collected on the middle pixel 2, while a pure induced signal was measured from the pixel 3, which collects no electrons.

The signal generated by the transient carriers has a characteristic shape: First it rises as the electron cloud approaches a pixel contact and then rapidly decrease as the carriers are being collected on neighboring pixels. A transient "kink", which comes first, is seen clearly in the waveform captured from the pixel 1, but it is completely masked by the collected-charge component in the waveform from pixel 2. Once all the carriers are collected or trapped in the bulk, the signals saturate to the levels proportional to the amounts of the collected charges, if we neglect the charge-signals induced by the trapped carriers, which are small due to the pixels' mutual shielding effect (small-pixel effect). For example, the signal from pixel 3 saturates to zero, meaning that no charge is being collected on that pixel. The heights of these levels give the information needed for the event reconstruction and evaluation of the total energy deposited by the incident photons.

2.3. Position sensing in local coordinate systems

As mentioned in the introduction, the signals generated on neighboring pixels can be used to refine the X-Y positions of interactions points to achieve sub-pixel resolution. Two approaches have been considered to enhance the spatial resolution in pixelated detectors by using the collected- and transient-charge signals generated in pixelated detectors. The first approach [8-10] is applied when the whole charge from the electron cloud is collected on a single pixel. In such cases, the electron cloud induces transient signals on the surrounding pixels with well-defined peaks, like the one shown in Fig. 2(c). Here, the amplitudes of the transient signals can be converted into X-Y coordinates of interaction points. It is clear that the signal generated on the central (collecting) pixel cannot be used, because its amplitude is not sensitive to position (i.e., it is propositional to the total collected charge only).

Theoretically, this approach should provide a sub-pixel resolution, but only within a geometrical area limited by the size of the electron cloud. The main drawback of this method is that the signals induced on neighboring pixels are rather weak. In addition, a strong electrostatic shielding by the central (collecting) pixel reduces the sensitivity of the non-collecting neighboring pixels to the locations of the electron clouds. The pixel sensitivity depends on the distance of the electron cloud to the anode, and it changes as the electron cloud drifts towards the multi-pixel anode side of the detector. If the cloud is far away, the signals induced on the nearby pixels will be very small. In the opposite case, when the electron cloud is very close to the central (collecting) pixel, it will be electrostatically shielded from the adjacent non-collecting pixels. The transient signals on the neighboring pixels reach their maxima when electron cloud comes at a certain distance from the anode. In contrast, the signal generated on the central pixel reaches its maximum when the electron cloud reaches the pixel. At this moment, the amplitudes of the transient signals are at zero levels. In other words, the measured amplitude of the collected-charge signal does not coincide in time with the measured amplitudes of the transient signals. This causes uncertainty in the reliance on the signal amplitudes for positional information. We note that our attempt to implement this approach for the detectors tested in this study was not fully successful.

The second approach is applied when the total charge from the electron cloud is shared between two or more neighboring pixels. The amounts of the collected charges correspond to the saturated levels of the signals. As in the previous approach, the signal amplitudes corresponding to these levels can be used to refine the positions of the interaction points with accuracy better than the pixel size, but, as in the previous case, within a certain geometrical area determined by the size of the electron cloud (to be discussed next). In reality, both types of events occur in pixelated detectors. The total charge from the electron cloud can be collected on a single pixel (single-pixel events), or it can be shared among several pixels (charge-sharing events). This means that both approaches should be combined to evaluate the coordinates of the interaction points in pixelated detectors.

Recently, Montemont *et al*. [11] demonstrated a novel algorithm for processing the waveforms captured after charge-sensitive preamplifiers to refine the positions of the interaction points. Its key feature is that it uses time-correlated (synchronized) samples of instantaneous amplitudes measured from several pixels regardless of whether the signals have a collecting or transient nature. The amplitudes stored in the waveforms measured from the neighboring pixels were used to evaluate the electron cloud position as it drifts towards the anode. Such estimates

can be done for every time slice of the waveforms, but there are optimal instances when the amplitudes are the most sensitive to the X-Y position.

In our studies we used an analog ASIC and relatively small pixels, so we focused on implementation of the charge-sharing approach to refine the positions of interactions. We defined a local coordinate system associated with each pixel. Fig. 3 shows 4 adjacent pixels, A, B, C, and D, for the conventional pixel pattern used in these measurements. The origin of the local coordinate system was placed in the middle of the upper left pixel, A, of each group of 4 pixels with the X- and Y-axes pointed, respectively, to the right and downward. By definition, all events for which the total produced charge is shared between pixel A and any combination of pixels B, C and D will be assigned to pixel A, i.e., the coordinate system associated with pixel A. Based on the amplitude of the captured signals, we separated the interaction events into 3 groups: (1) single-pixel events, i.e., those detected by the pixel A only, (2) double-pixel events, the total charge is shared between pixels A and B, or between pixels A and C, and (3) triple- and quadruple-events—the charge is shared between pixel A and any combination of two or three remaining pixels, B, C, and D. Accordingly, we call them 1-, 2-, and 3&4-pixel events (the triple- and quadruple-pixel events were processed identically). Obviously, for the 1-pixel events we cannot measure the position of the interaction point with better accuracy than the pixel pitch. This means that the pulse-height spectra measured for the 1-pixel events are collected over some area around the center of the pixel, and no further corrections can be applied. For the 2-pixel events, we could refine positions along the line connecting the centers between two adjacent pixels. Nevertheless, the pulse-height spectrum will be collected over some area between the two pixels. Only in the cases of 3- and 4-pixel events could we refine the positions within some areas over the corners of 4 pixels. The events from each of the groups are associated with particular geometrical regions in the X-Y plane. As an example, Fig. 3(b) illustrates the geometrical regions expected for a size of the electron cloud that equals 1/3 of the pixel size. If the diameter of an electron cloud corresponds to a pixel size, then the region of single-pixel events shrinks to a point, the double-pixel-events region collapses into a line, while the region of quadruple-pixel events region expands to its maximum size that equals the size of the pixel. In the extreme case, when an electron cloud's size is zero, the double- and quadruple-pixel event areas disappear completely, while the region of the single-pixel events expands over the entire area of the pixel. A combined area of all four regions always corresponds to the pixel's area, regardless of the size of the electron cloud provided that the cloud's size remains smaller than the pixel's size,

which was the case in this work. This allowed us to analyze data and to apply corrections for each pixel individually, using its uniquely assigned local coordinate system. For each pixel and each group of the events, we evaluated the local pulse-height spectra, which we then used to plot the overall spectra for single-, double- and quadruple-pixel events.

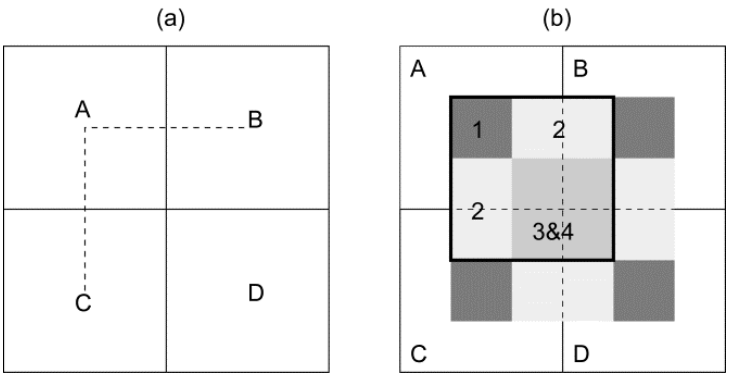

Fig. 3. Local coordinate system assigned to the pixels: Conventional (a) and (b). The origin of the coordinate system is in the middle of the upper left pixel, A, of each group of 4 pixels with the X- and Y-axis pointed to the rightward and downward, respectively. The grey-colored squares in (b) illustrate locations of 1-, 2-, and 3&4-pixel events. The dashed lines in (a) show locations assigned to the 2-pixel events.

In accordance with the above classification, the positions of the 1-pixel events were assigned to the center of pixel A, 2-pixel events were placed along the lines connecting the centers of the pixels (A,B) and (A,C), whilst 3- and 4-pixel events were placed within the square regions (or the tilted parallelepiped in the case of the shifted row pattern) centered over the corners of four adjacent pixels, respectively (see Figs. 3(a) and (b)). For 3&4-pixel events, we applied the Center of Gravity Method to calculate the location of each interaction point within the above regions.

Since the size of the electron cloud depends on the drift time, the multi-pixel events interacting at different depths will be assigned to the different geometrical areas of the detector. This feature should be taken into account when evaluating the real positions of the interaction points, but it is not important for charge-loss corrections since the correction applied depends on the interaction depth.

2.4. Device calibration and signal processing

The goal of the calibration is to find 1-, 2-, or 3-dimensional matrices, corresponding to 1-, 2-, and 3&4-pixel events, that will be used to correct the measured signals generated from particular voxels. Each region associated with a particular pixel (as described in the previous section) has its three matrices taking into account the electronic gain and signal variations due to the charge-losses and transient signals. The latter two variables correlate with the x-y-z coordinates of the voxels. In general, we should have considered the energy dependence of the above matrices. However, in this work we used a single 662-keV gamma-ray line.

The calibration was done in two steps. We used an un-collimated ^{137}Cs source to generate the output signals from the pixels. Using these data, we plotted, for each pixel (anode), the dependencies of the captured peaks versus drift-times and used these dependences to equalize the pixel responses along the Z-direction by fitting the center of gravity of the photopeak continuums with polynomial functions. We used these functions to correct the measured amplitudes. Then, we evaluated the corrected pulse-height spectra for each of the pixels and equalized the pixel gains by aligning the right edges of the 662-keV photopeaks. This is a basic correction technique typically employed for all types of CZT detectors to equalize the detector's response along Z-direction, and to calibrate the gains of each detector's channel.

The second-order corrections were based on the location of each interaction point.

For the single-pixel events, no additional corrections are possible. In the case of the 1.4-mm pixel detectors, the majority of the events are single-pixel, which means that the detector's overall response and its energy resolution can be corrected on the scale of the pixel size.

For multiple-pixel events, we applied the Center of Gravity Method to evaluate the local positions of the interaction points along the lines connecting the centers of the corresponding pixels (2-pixel events), or inside the areas covering four adjacent pixels (3&4-pixel events). In addition, we used the drift times (evaluated via the timing information measured for those signals with the highest amplitude) to find the location of the interaction point along the Z coordinate. Knowing these coordinates, we could sort the events in accordance with the locations of the interaction points. To do this, we divided the lines connecting the centers of the two adjacent pixels: (A-B) and (A-C) into N segments, and the area between the lines connecting centers for four pixels into N^2 sub-pixels. The

thickness of the detector was divided into 25 segments corresponding to 0.4-mm segments in the Z direction. The events from each voxel were process separately: Amplitudes (after the first-order corrections) captured from adjacent pixels were added, and the resulting amplitudes were used to generate the pulse-height spectra, from which the peak positions were used to equalize the detector's response. By equalizing the responses from each voxel, we corrected the effects responsible for the variations in response that were (1) due to crystal defects, (2) due to transient signals, and (3) due to the fact that summing the signals from two or more adjacent pixels significantly reduces the detectors shielding efficiency (small pixel effect). Normally, we acquired two data files, one for calibrating the response matrix, and the second for plotting the pulse-height spectra and evaluating the photopeak width (% FWHM at 662 keV).

The peak widths were evaluated from Gaussian fits. Since the peaks obtained after the drift-time corrections are not represented exactly by a Gaussian function, we also calculated their geometrical width at half the maxima. We note that for Gaussian fitting, we selected the fitting interval defined by two levels relative to the peak's height as 0.3 on the left side, and 0.2 on the right.

2.5. Identifying the collected-charge signals

The transient signals induced on adjacent pixels may significantly degrade the device's performance especially when conventional (analog) signal processing is used. Fig. 2 illustrates the charge signals (waveforms) measured after the charge-sensitive preamplifiers from three adjacent pixels, corresponding to a double-pixel event when only two pixels share the electron cloud: pixels 1 and 2 in this case. The signal captured from the pixel 3 is a pure induced (transient) signal. These waveforms were measured with our previously tested detector with a pixel size of 2 mm.

Because of charge sharing, the waveform measured from pixels 1 and 2 can be considered as a superposition of the collected- and the induced-charge signals generated, respectively, by the collected and transient carriers. In the example shown in Fig. 3, the majority of the charge was collected on the middle pixel 2, while a pure induced signal was measured from the pixel 3, which collects no electrons.

The signal generated by the transient carriers has a characteristic shape: First it rises as the electron cloud approaches a pixel contact and then rapidly decrease as the carriers are being collected on neighboring pixels. A

transient “kink”, which comes first, is seen clearly in the waveform captured from the pixel 1, but it is completely masked by the collected-charge component in the waveform from pixel 2. Once all the carriers are collected or trapped in the bulk, the signals saturate to the levels proportional to the amounts of the collected charges, if we neglect the charge-signals induced by the trapped carriers, which are small due to the pixels’ mutual shielding effect (small-pixel effect). For example, the signal from pixel 3 saturates to zero, meaning that no charge is being collected on that pixel. The heights of these levels give the information needed for the event reconstruction and evaluation of the total energy deposited by the incident photons.

As we described before, the H3D ASIC employs conventional analog pulse-processing based on signal shaping, i.e., it averages the charge signals over a certain interval (shaping time). As a result, both the collected- and transient-charge components contribute to the resulting filtered amplitudes of the peak, and its timings measured by the ASIC. The ASIC’s shaping amplifiers generate positive unipolar signals in response to the positive slopes of the charge-signals read out from preamplifiers and the negative ones in response to the negative slopes. The pure collected-charge signals have only positive slopes, while the transient signals have both. The ASIC has an ability to capture both the positive and negative amplitudes of the anode signals. The latter provides additional information for the event reconstruction.

A detailed description of how the signals are generated in the 3D pixelated detectors was given by Zhang *et al*. [18]. However, it is important to mention that the shaped transient signals always reach their maxima earlier than do the collected-charge ones, a feature that can be used for distinguishing between them. Uncertainties introduced by the transient signals can degrade the performance of pixelated detectors, especially when analog ASICs are used. Digital pulse-processing based on the numerical fitting of the waveforms captured after charge-sensitive preamplifiers would help to minimize these problems.

The ability to measure the signal amplitudes corresponding to the collected charges is critical for reconstructing events in pixelated detectors. The information on amplitude and timing for each event must be combined to identify the pixels of interest, evaluate the amounts of the collected charges and the corresponding drift times, apply corrections, and, finally, add amplitudes together to find the total energy deposited by the incident particle.

A straightforward way to identify the hit pixel, i.e., the pixels that actually collected the charge, is by checking if the signal goes above the noise level. However, this alone cannot distinguish between the true collected charge and

transient signals, in particularly in the case of the charge sharing when both types of signals are superimposed on each other. The timing information and presence of the negative peaks in the anode signals helps with the identification in such cases.

As was described above, the ASIC provides the timing corresponding to positive and negative peaks captured from the anodes and the cathode. Since only positive amplitudes can generate trigger events in a data analysis we use timing information corresponding to the positive peaks. The fast-shaped (200-ns peaking time) cathode signal gives their starting point, while positive peaks of the long-shaped (1-μs peaking time) anode signals correspond to the electron cloud's arrival time at the pixel contacts (except for the transient signals). Both times are measured with respect to a common start issued by the triggered pixel after a hardware-selected delay. The anode times allow chronological ordering of the arrivals of the anode peaks, while differences between the anode- and cathode-times give the electron clouds' drift times.

Correlations between the amplitudes measured from two or more adjacent pixels and between the times and amplitudes captured from a single pixel can provide valuable information about the performance of pixelated detectors and readout electronics. Accordingly, we call them (A-A) and (A-T) correlations. To illustrate how timing information can help to identify transient signals and to avoid adding transient amplitudes to the total output signal, we plot the amplitude-time (A-T) correlation for a selected pixel. A detector was irradiated by gamma rays from an uncollimated ^{137}Cs source. Fig. 4 shows the correlation plotted in the normal- (a) and x10- (b) scales. The events were triggered by any one of the 121 detector pixels. To preserve the natural chronological order of the captured amplitudes, we subtracted the ASIC-provided times from a reference time selected for convenience. The scales of the reference time and the peak- and time-scaling factors were chosen to fit the (A-T) distributions within a 500-channel range. The signals' base levels were placed at a channel 50.

A sharp peak around channel 250 represents the events triggered by the pixel itself. Accordingly, all the peaks captured before the trigger (events on the left) have amplitudes below the hardware's threshold (dashed line in Fig. 4(b)). The dots on the right correspond to the events triggered by other pixels. The amplitude of the trigger peak corresponds to the maximum energy of the gamma rays, in this case 662 keV.

A narrow branch (curvature) of dots emerging on the right side of the trigger peak represents the photopeak (total energy absorption) events for which the total charge is shared with one of the neighboring pixels that

generates the trigger. This branch illustrates the time delays measured for the amplitudes of the shaped signal affected by the transient signals during the charge sharing. Although the shared charges arrive at adjacent anodes almost simultaneously, the amplifier-shaped signals reach their maxima at different moments. The stronger the contribution of the transient component, the sooner the shaped signal reaches its maximum. Conversely, when the transient signals are becoming small in comparison to the collected-charge ones, then the time readings from the pixels that shared the charge are nearly the same. That is why the curvature smoothly merges with the trigger's peak. It should reappear on the left side provided that the correct trigger conditions are selected.

The dots on the left side of the trigger peak are associated with two kinds of signals: (1) Induced by transient carriers, and, (2) there is superposition of the transient and low-amplitude collected-charge signals generated during the charge sharing. The deep dark continuum on the left of the trigger peak in Fig. 4(b) corresponds to the pure transient signals, while the grayish continuum corresponds to the superposition of the collected charge- and transient-signals. The amplitudes of the time-independent noise also can be seen on the right side. These details are very important for optimizing the event processing and applying signal corrections.

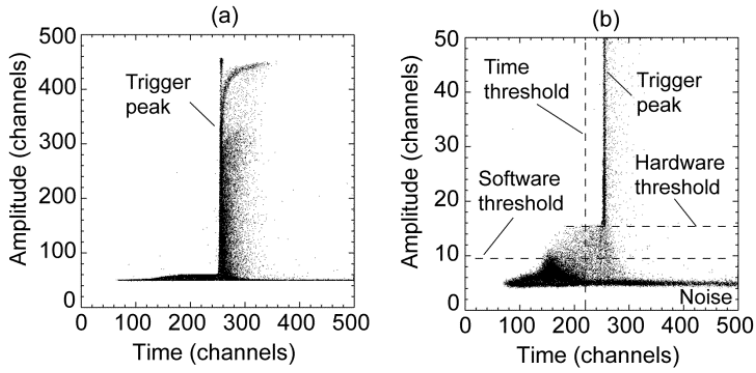

Fig. 4. The (A-T) correlation plotted in the normal- (a) and x10- (b) scales. The events were triggered by any of the 121 detector pixels.

Fig. 5 (a) shows the (A-T) correlations of the events acquired from 3x3 adjacent pixels. Herein, the events were triggered by a central pixel 24, which means that the charge is shared between pixel 24 and one or several surrounding pixels. As shown, the correlations plotted for pixels having common sides with pixel 24 are similar to the one shown in Fig. 4, while the correlations plotted for the diagonal pixels, as we expected, have no features corresponding to the double-pixel events. Fig. 5(b) depicts the amplitude (A-A) correlations plotted for the same pixels, and the pulse-height spectrum for the central pixel. We note that zero amplitude corresponds to channel 50.

In each plot, the coordinate axes represent the amplitudes captured from the central pixel and one of the adjacent ones. The distributions of the narrow dots parallel to the Y-axis correspond to single-pixel events, i.e., all the charge is collected on the central pixel. Conversely, the single-pixel events detected by the neighboring pixels are not present in the plots because of the threshold set for the central pixel. For pairs of pixels with joint sides, one can see a narrow distribution of dots following the lines located at 45 degrees with respect to the coordinate axes. These distributions also represent the photoabsorption events, but now, the total deposited charge is shared between these two pixels. Our goal in showing these (A-A) correlations was to demonstrate that there are no such features in the distributions plotted for the diagonal pixels, since the charge is shared between three or four pixels. An important feature seen in Fig. 5(b) is that the distributions of the photoabsorption events show no bending (except for barely visible bending at the very ends of the distributions), signifying that there are no significant charge losses in the gaps between the pixels.

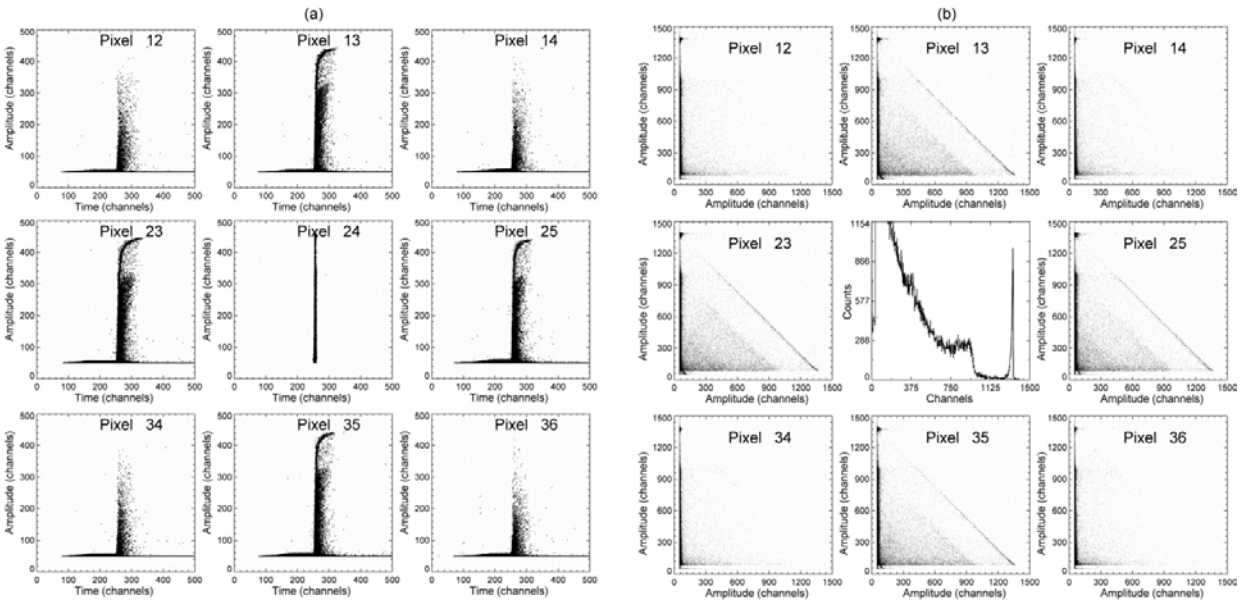

Fig. 5. The (A-T) (a) and (A-A) (b) correlations of the events acquired from a 3x3 array of adjacent pixels. The events were triggered by the central pixel 24 to which the uncorrected pulse-height spectrum corresponds.

During the data analysis, we used the above (A-T) correlations to identify the pixels of interest by rejecting those signals that do not satisfy certain criteria. Thus, we reject the pixels generated by transient signals, located in the area below the energy threshold and on the left of the time threshold. We also reject pixels whose signals were

below the noise level. Finally, we applied rejection criteria based on the geometrically allowable combinations of the pixels. It is important to bear in mind that the above approach is not ideal. Some signals will be incorrectly identified, causing low- and high-energy tails for the photopeaks. By slightly changing thresholds we can control the fractions of the single-, double-events and quadruple-events. For example, the events from the low-energy photopeak tail in Fig. 5(b) could be redistributed to the double-pixel events, so improving the energy resolution of the single-pixel peak. But, at the same time, this will broaden the double-pixel peak if the events were incorrectly identified, and vice versa. It means that, in the general case, global optimization is required to achieve the best resolution for the combined spectra of all events.

Since the size of the electron cloud depends on the drift time, the multi-pixel events interacting at different depths will be assigned to the different geometrical areas of the detector. This should be taken into account when evaluating the real positions of the interaction points, but it is not important for charge-loss corrections since the applied correction depends only on the depth of interaction.

3. Results and discussion

The goal of this work was to demonstrate the feasibility of using high-granularity position sensing to correct non-uniformities in the response of CZT pixelated detectors. We did not consider here other important aspects related to pixelated detectors, many of which have been previously discussed in the literature [11-18].

3.1. Performance baseline

As was described in Section 2, first we evaluated the 1.4-mm pixel size detectors and used their performances as the baselines for comparing the improvements in response achieved in the next runs of measurements. We applied the drift-time corrections for each of the pixels, and separately evaluated the pulse-height spectra for the single-, double- and quadruple-pixel events. We note that the majority of the interactions in these detectors produced single-pixel events, whose energy spectra were used as a measure of the detectors' baseline performances.

Fig. 6 shows the comparisons between the X-ray diffraction topography images of the top and the bottom surfaces of the four CZT crystals used to fabricate the detectors, and the corresponding pulse-height spectra. The

spectra were taken at a 2000-V bias except for detector 4 for which we were able to apply 1800 V only, because of the high electronic noise caused by leakage current in this detector.

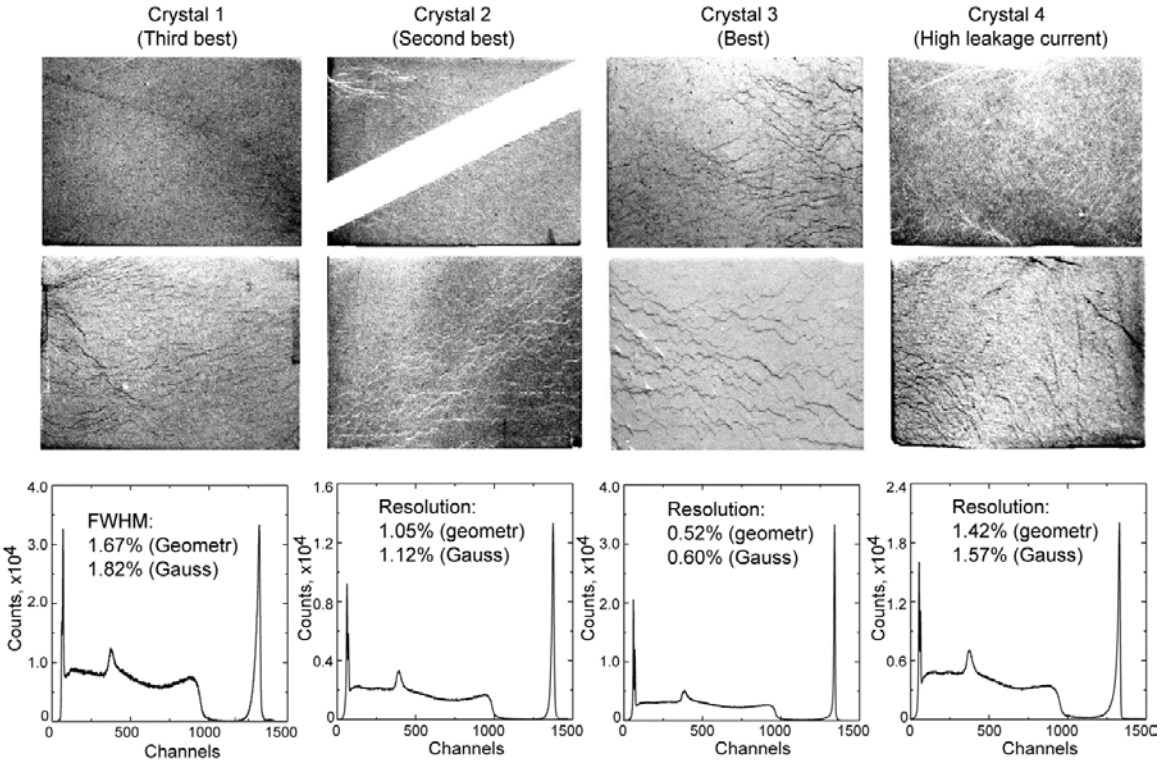

Fig. 6. Correlations between the X-ray diffraction topography images of the top and the bottom surfaces of the CZT crystals, and the corresponding pulse-height spectra. Crystal 2 has twin boundaries.

As seen from Fig. 6, among the four detectors, number 3 shows the best response with a spectral resolution of <0.6% FWHM at 662 keV, while the remaining ones show just modest performance, despite the fact that there are not many differences in the X-ray diffraction images, which revealed high concentrations of subgrain boundaries and Te inclusions inside the crystals. They all look more or less the same, except for number 4, containing several distinct high-dislocation-density subgrain boundaries that likely cause the high leakage-current noise observed for this detector. We note that after re-fabrications, the leakage current of this crystal increased dramatically, preventing us from using it in the next runs of measurements. The lack of an obvious correlation between the detectors' responses and the diffraction topography data suggests that the walls of dislocations present inside the subgrain boundaries do not dominate the electron transport. However, they may be responsible for the spatial variations of the trapping centers (impurities and native point-defects) accumulated around the dislocations, which, in turn, cause

non-uniform charge collection. On the other hand, number 1 has a very pronounced subgrain boundary crossing the crystal from one corner to another, while number 2 is very similar to number 3, but it has twin boundaries decorated by Te inclusions.

Despite the presence of the network of subgrain boundaries, detector 3 shows an outstanding performance. It also illustrates our ability to use the advantages of the H3D ASIC for reading signals from pixelated detectors, and correctly processing the data. Fig. 7 plots the best combined spectrum from all pixels (except for the peripheral ones) after equalizing the photopeak positions. The energy resolution was evaluated using two different methods: Gaussian fitting gave 0.53%, and direct measuring of the photopeak width gave 0.45%. Both results demonstrate outstanding performance of the detector and the electronics. We note that a Gaussian fitting always gives slightly bigger estimates because of the low-energy tailing effect, which is a consequence of analog-signal processing: In the transition region from single- to double-pixel events, some events always are misidentified. Also, we note that this spectrum is slightly better than the corresponding spectrum shown in Fig. 6. As we described at the end of the Section 2.5 the corrected spectra slightly depends on the selected criteria for identification of the events multiplicity. It the latter case they were tuned better.

Based on the spectral performance we rated the crystals: Crystal 3 gave the best performance, the second best is number 2, and the third is number 1. We did not carry out further measurements with detectors fabricated from crystal 4, because all refabricated detectors had high noise above 1200 V.

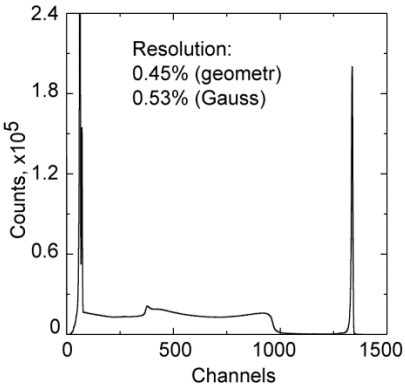

Fig. 7. Combined spectrum of single-pixel events measured for the detector fabricated from the best crystal.

3.2. Detectors fabricated from the best crystal

Here we summarize the results from testing three detectors with different pixel sizes fabricated from the best crystal (crystal 3). Since the performance of this crystal even in the 1.4-mm pixel configuration was very close to its statistical limit, we did not anticipate further improvement by increasing the device's segmentation.

Fig. 8 shows the dependence of the energy resolution, evaluated for double- and quadruple-pixel sharing events, on the linear number of segments, N. We recall that for the multiple-pixel events, we applied further corrections in the response by segmenting the detector area into N^2 segments, as described in Section 2.3. The dashed lines represent the energy resolution, measured for the single-pixel events, for which we could not refine the locations of the interaction points and apply corrections. Because of the high uniformity in the response of crystal 3, we obtained ~0.5% FWHM at 662 keV for single-pixel events, regardless of the pixels' sizes.

At first glance, it is surprising that the energy resolution measured for the multiple charge-sharing events is significantly worse than that measured for the single-pixel events. As we explained in Section 2.3, the broadening of the photopeaks is caused by the transient signals. However, the variations caused by the transient signals can be treated the same way as the variations caused by the crystal's defects. Both correlate to the locations of the interaction points and, thus, can be corrected by segmenting the detector, as is evident in the curves plotted for double- and quadruple-pixel events. At the higher granularity (or higher segmentation), the energy resolution improves and approaches the level achieved for the single-pixel events. We note that, as expected, the contribution of the transient signals falls with decreasing the pixel size and the multiplicity of the charge-sharing pixels.

The results from testing these detectors demonstrate that in crystals with a highly uniform response, high-granularity sensing has little or no advantage over the current 3D devices in terms of energy resolution. However, it is expected to improve the detector's spatial resolution, which is beneficial for reconstructing Compton events and for many gamma-ray imaging applications utilizing CZT. A detector with a pixel size of 1.5 mm seems to be a good compromise for getting the best energy resolution by minimizing a fraction of the charge-sharing in the case of 10-mm thick high-uniformity detectors. For those 15-mm thick detectors, the optimum size will be slightly bigger to accommodate larger sizes of electron clouds. From this point of view, a 1.7-mm pixel size, as used by Z. He's team from the University of Michigan for their 3D devices [2], is an excellent choice when high-quality crystals are used.

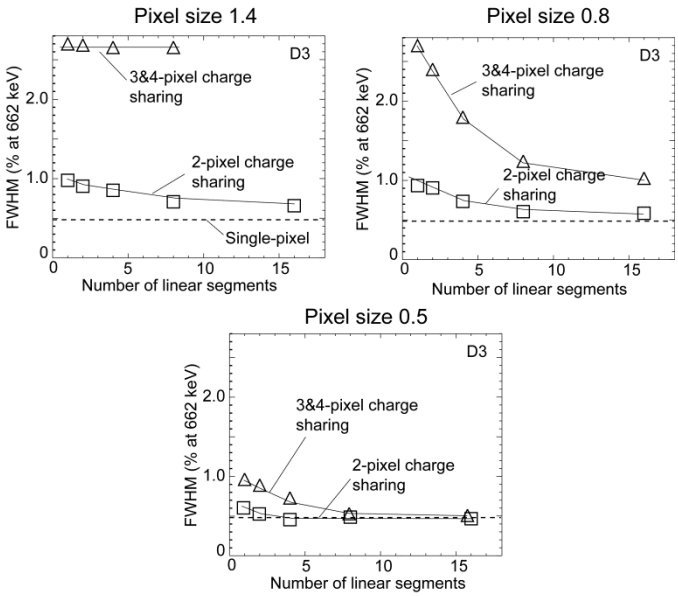

Fig. 8. Dependence of energy resolution evaluated for the detectors fabricated from the best CZT crystal (crystal 3).

Fig. 9 compares the combined (all-pixels) spectra for single- and quadruple-pixel events measured, respectively, from the 1.4- and 0.5-mm pixel detectors. As seen, adding the amplitudes from four neighboring pixels for the 0.5-mm pixel size detector, has little effect on the energy resolution, meaning that detectors with ~0.5-mm pixel size is a good choice for making high-granularity pixelated detectors.

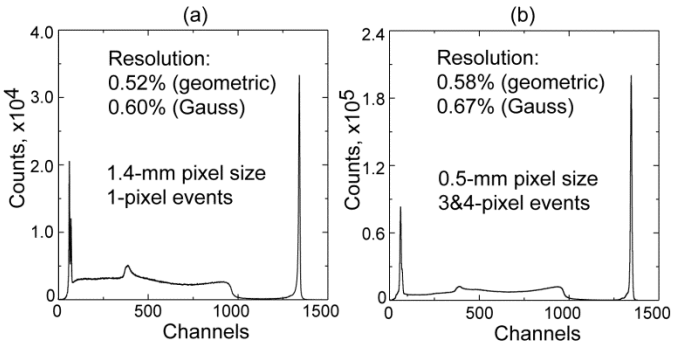

Fig. 9. Comparison between the combined (all-pixel) spectra for single- and quadruple-pixel events measured from the 1.4- and 0.5-mm pixel detectors, respectively.

3.3. Detectors fabricated from the second best crystal

All our previous comments are fully relevant to our second set of data obtained from testing detectors made from the second best crystal (crystal 2). As in the previous case, we first measured the baseline response from the 1.4-mm

pixel sized device. The energy resolution for single-pixel events was 1.2% (indicated by a dashed line in the plots), which is ~2 times greater than that measured in the best crystal, meaning that the uniformity of the response of this crystal is not satisfactory, i.e., such a crystal should not be used for making a 3D device.

Fig. 10 illustrates how the response's non-uniformities can be corrected by using high-granularity position sensing. Thus, the energy resolution improved when we selected the charge-sharing events and applied additional corrections based on fine device segmentation. Particularly, significant improvements can be seen for the 0.5-mm pixel detector; we achieved <0.7% resolution for both double- and quadruple-pixel events. These results demonstrate that the high-granularity pixelated detectors support accurate correction of non-uniformities in the response, and makes possible to use CZT crystals that otherwise would be rejected. In this particular case, we achieved sub-percent energy resolution from the crystal that would not be acceptable for making 3D pixelated detectors. We note that for the single-pixel events, the resolution improves just a little, from 1.2% to 1.1%, when the pixel size decreases from 1.4- to 0.5-mm, meaning the 0.5-mm spatial resolution is not sufficient to fully correct the response non-uniformities.

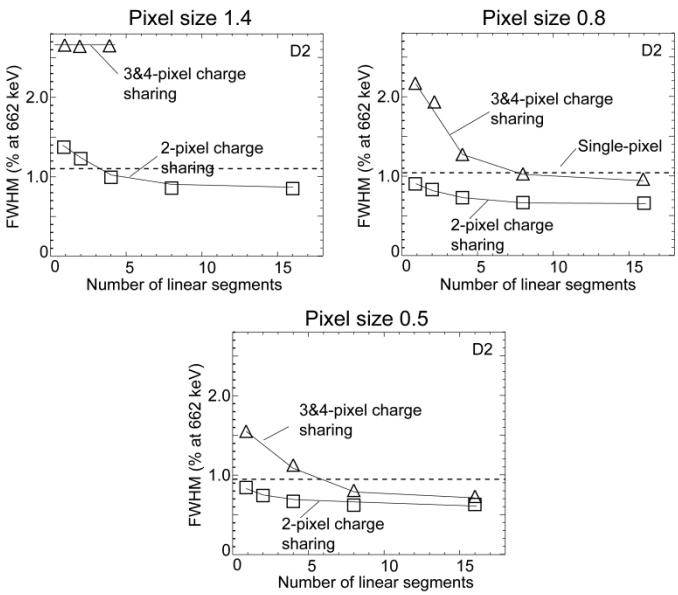

Fig. 10. Energy resolution evaluated for the detectors fabricated using the second best crystal (crystal 2).

3.4. Detectors fabricated from the third best crystal

Fig. 11 shows the results obtained for the third best crystal (crystal 1). For the reason explained below, we believe that the detectors fabricated from this crystal had significant variations in the local electric field near the

pixel contacts that caused difficulties in identifying the multiplicity of charge-sharing events and measurements of the fractions of shared charge. The energy resolution and fraction of the photopeak events measured for all three detectors fabricated from this crystal particularly were sensitive to the energy- and time-thresholds for identifying the charge-sharing events, especially in the case of the 1.4-mm pixel detectors with strongest contribution by the transient signals. For example, for the 1.4-mm pixel detector, the energy resolution measured for single-pixel events was between 1.7- and 2.6-% at 662 keV, dependent on the selected thresholds. By setting a higher energy threshold, we could improve energy resolution for the single-pixel events, but it entailed a greater fraction of the transient-affected events being added to the double- and quadruplet-pixel spectra, which degrades their photopeaks. That is why a global optimization of such detectors is necessary to set the optimal thresholds. Because of the narrow scope of this work, we did not carry out a full optimization study. Instead, we selected the thresholds to achieve the best energy resolution for the single-pixel events, in the case of the 1.4-mm pixel detector which had a majority of single-pixel events, and for the quadruple-pixel events, in the case of the 0.8- and 0.5-mm pixel detectors. We note that this problem would be almost eliminated if digital pulse-processing were used. This result also highlights the limitations of using the charge-sharing approach for position sensing, not only because the area for which the position information available is limited by the size of the electron cloud, it also is too sensitive even to small variations of the electric field near the pixels. Use of non- collecting charge-sensing strips would be a better approach for position sensing in pixelated detectors.

Fig. 13 shows the combined pulse-height spectra measured for the detectors fabricated from the third-best crystal. The first spectrum (top) was measured for the 1.4-mm pixel size detector (baseline performance). Here, the majority of the events are single-pixel events for which we applied only a drift-time correction. The energy resolution was ~3% at 662 keV. The plots at the bottom show the spectra obtained for the 0.5-mm pixel detector: Single-pixel events (left), two-pixel events (middle), and 3- and 4-pixel events (right) are shown. As seen, in all cases the resolution improves below 1.3%, i.e., another confirmation of the value of high-granularity detectors. Despite segmenting this detector down to 100-μm voxels, we were unable to achieve sub-percent resolution. We think this is because of the strong variations of the local electric field near the anode, which can be overcome by applying higher electric fields. This is one of the reasons why the 3D detectors usually require high bias voltage for their operation.

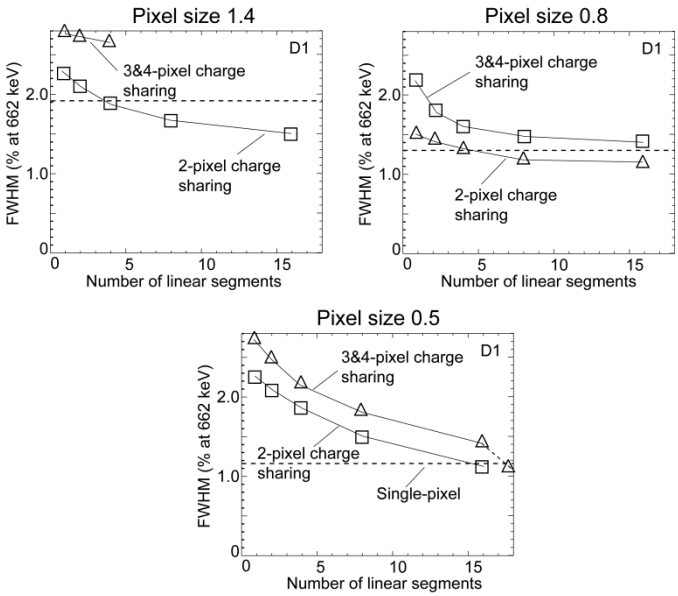

Fig. 11. Energy resolution evaluated for the detectors fabricated using the second best crystal (crystal 1).

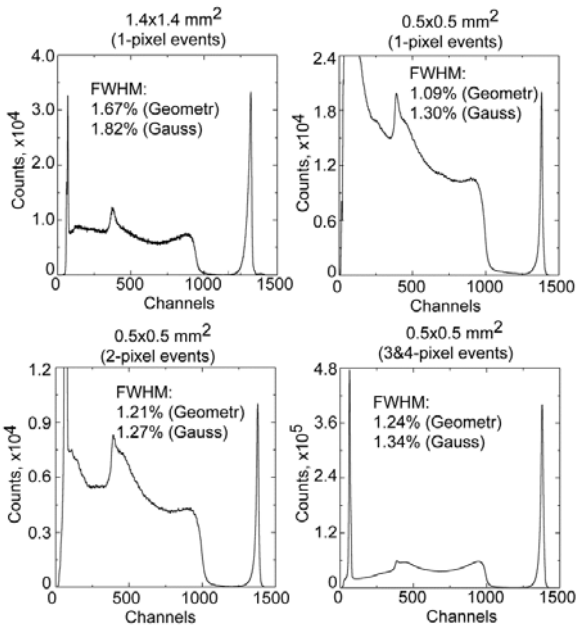

Fig. 12. Improvements in the energy resolution of the poor CZT crystal using a high-granularity 3D pixelated detector with a pixel size of 0.5 mm. The first spectrum (top) was measured for the 1.4-mm pixel size detector (baseline performance).

It is clearly seen that the contribution of the transient signals decreases, which supported better correction of their effects. But we are still prevented from achieving the single-pixel limit in the case of 3- and 4-pixel sharing events. Only when we make a detector with 0.5-mm pixel size were we able to achieve a better energy resolution.

4. Conclusions

The basic concept behind high-granularity detectors is to measure the locations of interaction points with high spatial resolution and accordingly correct the measured charge signals generated from these locations. By using the high-resolution position sensing, we demonstrated the enhancement in the response of the detectors fabricated from unselected CZT crystals.

We investigated the spectral responses of 15x15x10 mm^3 pixelated detectors fabricated with progressively smaller pixel sizes: 1.4, 0.8, and 0.5 mm. In each run of measurements, we tested 4 detectors (with the same pixel sizes) fabricated from the 4 CZT crystals, which were used in the next runs.

The detectors fabricated from the best crystal (crystal 3) showed excellent performance, with the energy resolution only being limited by the electronic noise and electron-hole pair production statistics, regardless of the pixel size, implying that in this case of a crystal with a highly uniform detector response, no further corrections are required. The pixel size, ~1.7 mm, currently used for 3D pixelated detectors, seems a nearly optimal choice for crystals with high response homogeneity. However, the production yield of such crystals is low, while their cost is high.

For the second best crystal (crystal 2), we found that when the pixel size decreases from 1.4 mm to 0.5 mm, we were able to apply an accurate correction based on the charge sharing between 3- and 4-adjacent pixels and so improve the energy resolution from ~1.5% down to 0.7%. Furthermore, based on the pulse-height spectra for 1- and 3&4-pixel events, we conclude that adding together signals from 3- or 4-pixels does not increase significantly the electronic noise in the case of 0.5-mm pixels.

These results demonstrated that enhancements of CZT pixelated detectors fabricated from unselected material are possible by using high-granularity position sensing, in agreement with our previous results from position-sensitive virtual Frisch-grid detectors.

However, the reliance on charge sharing is not necessarily the best approach for measuring the positions of the interaction points in pixelated detectors. Its limitations were revealed as we tested detectors fabricated from the third best crystal (crystal 1). In this case, we also improved its energy resolution compared to the performance baseline, viz., another confirmation of the advantage of the high-granularity detectors. However, even after segmenting the detector down to 100-μm voxels, we were unable to achieve sub-1% energy resolution as in the previous two crystals. We can explain this failure as reflecting the strong distortions of the local electric field caused by crystal defects, particularly those near the anode. Such variations, even small ones, can affect the charge sharing and consequently, introduce significant errors in the position measurements.

We evaluated the performance of the H3D ASIC for pixelated detectors with small pixel sizes or a large fraction of charge-sharing events. Its main limitation comes from using the conventional analog-pulse processing, based on the shaping of the anode signals. The information provided by the ASIC is insufficient to distinguish confidently between the collected charge and transient signals in the charge-sharing events, particularly when a small fraction of the total charge is collected on one of the pixels. It means that then, we can neither identify correctly the pixels that collect charge nor the true amounts of the collected charge. For example, 1-pixel events could be assigned incorrectly as 2-pixel ones and vice versa. This introduces additional variations, which degrades the energy resolution. Even by slightly changing the time and energy thresholds, we can relocate events between the groups with different pixel multiplicities, so affecting the spectral responses evaluated for each of these groups. Digital pulse-processing based on fitting the waveform signals after the charge-sensitive preamplifiers, which contain information on the true charges collected on the pixels, would eliminate these problems.

To increase the acceptance yields of today's CZT crystals, we have to implement device designs able to correct non-uniformities in detector response on a small scale, at least on a scale comparable to the size of electron clouds. This opens up the opportunity to use off-the-shelf unselected CZT crystals at a reduced cost, while still achieving the sub-percent energy resolution for the majority of them.

Another important finding is that the conventional pixelated detectors similar to 3D pixelated devices proposed by the University of Michigan but with small pixel sizes, <0.5 mm, can provide the high-granularity segmentation by using charge sharing between several adjacent pixels. However, this approach has two drawbacks: (1) it requires a large number of readout channels, and (2) the charge sharing may be too sensitive to the local variation of the

electric field near the anodes. We believe that the novel pixel patterns featuring large pixels, 2-3 mm, and position-sensing strips will eliminate both of these problems.

Acknowledgments

This work was supported by U.S. Department of Energy, Office of Defense Nuclear Nonproliferation Research & Development (DNN R&D). The manuscript has been authored by Brookhaven Science Associates, LLC under Contract No. DE-AC02-98CH1-886 with the U. S. Department of Energy.

References

[1] G. Knoll, Radiation Detection and Measurement, 4th ed., Wiley, 2010.

[2] Z. He, W. Li, G. E Knoll, D. K. Wehe, J. Berry, C. M. Stahle, “3-D position sensitive CdZnTe gamma-ray spectrometers”, Nucl. Instr and Meth. A422, pp. 173-178, 1999.

[3] Li, W.; He, Z.; Knoll, G.F.; Wehe, D.K.; Berry, J.E. A data acquisition and processing system for 3D position sensitive CZT gamma-ray spectrometers. *IEEE Trans. Nucl. Sci.*, *46*, 1989–1994, 1999.

[4] Y.F. Du, Z. He, G.F. Knoll, D.K. Wehe, W. Li, “Evaluation of a Compton scattering camera using 3-D position sensitive CdZnTe detectors”, Nucl. Instrum. Methods Phys. Res. A, 457,203–211, 2001.

[5] A. E. Bolotnikov, G. S. Camarda, Y. Cui, G. De Geronimo, J. Fried, A. Hossain, K. Lee, G. Mahler, M. Maritato, M. Marshall, M. Petryk, U. Roy, E. Vernon, G. Yang and R. B. James, “Use of high-granularity position sensing to correct response non-uniformities of CdZnTe detectors”, Appl. Phys. Lett. 104, p. 263503, 2014.

[6] M. A. J. van Pamelen and C. Budtz-Jørgensen, ”Novel electrode geometry to improve the performance of CdZnTe detectors”, Nucl. Instr. and Meth. A 403, pp. 390-398, 1997.

[7] I. Kuvvetli, C. Budtz-Jørgensen, E. Caroli, N. Auricchio, “CZT drift strip detectors for high energy astrophysics”, Nucl. Instr. and Meth. A 624, pp. 486-491, 2010.

[8] W. Warburton, “An approach to sub-pixel spatial resolution in room temperature X-ray detector arrays with good energy resolution,” in *Proc. Materials Research Soc. Symp.*, 1997, vol. 487, pp. 531–536.

[9] T. Narita, J. E. Grinddlay, J. Hong, and F. C. Niestemski, Proc. SPIE 5165, X-Ray and Gamma-Ray Instrumentation for Astronomy XIII. 5165, pp. 542-643, 2004.

[10] Y. Zhu, S. E. Anderson, and Z. He, “Sub-Pixel Position Sensing for Pixelated, 3-D Position Sensitive, Wide Band-Gap, Semiconductor, Gamma-Ray Detectors”, IEEE Trans. Nucl. Sci., Vol. 58, no. 3, pp. 1400-1409, 2011.

[11] G. Montémont, S. Lux, O. Monnet, S. Stanchina, and L. Verger, “Studying Spatial Resolution of CZT Detectors Using Sub-Pixel Positioning for SPECT”, IEEE Trans. Nucl. Sci., Vol. 61, no. 5, pp. 2559–2266, 2014.

[12] F. Zhang, Z. He, G. F. Knoll, D. K. Wehe, and J. E. Berry, “3D position sensitive CdZnTe spectrometer performance using third generation VAS/TAT readout electronics,” IEEE Trans. Nucl. Sci., Vol. 52, no. 5, pp. 2009–2016, 2005.

[13] G. De Geronimo, E. Vernon, K. Ackley, A. Dragone, J. Fried, P. O’Connor, Z. He, C. Herman and F. Zhang, “Readout ASIC for 3D Position-Sensitive Detectors”, IEEE Trans. Nucl. Sci., Vol. 55, no. 3, pp. 1593-1603, 2008.

[14] E. Vernon, K. Ackley, G. De Geronimo, J. Fried, P. O’Connor, Z. He, C. Herman, and F. Zhang, “ASIC for high rate 3-D position sensitive detectors,” IEEE Trans. Nucl. Sci., vol. 57, no. 3, pp. 1536-1542, 2010.

[15] F. Zhang, C. Herman, Z. He, G. De Geronimo, E. Vernon, and J. Fried, “Characterization of the H3D ASIC readout system and 6.0 cm^3 3-D position sensitive CdZnTe Detectors,” IEEE Trans. Nucl. Sci., Vol. 59, pp. 236-242, 2012.

[16] C. Szeles, S.E. Cameron, S.A. Soldner, J.-O. Ndap, and M.D. Reed, J. Electr. Materials, 33(6), pp. 742-752, 2004.

[17] A. E. Bolotnikov, J. Butcher, G. S. Camarda, Y. Cui, G. De Geronimo, J. Fried, A. Hossain, K. H. Kim, M. Marshall, M. Petryk, E. Vernon, G. Yang, and R. B. James, “Comparison of analog and digital readout electronics on the processing of charge-sharing events in pixelated CdZnTe detectors”, IEEE Trans. on Nucl. Science, Vol. 61, Issue 2, pp. 787-792, 2014.

[18] F. Zhang, W. R. Kaye, and Z. He, “Performance of 3-D Position Sensitive CdZnTe Detectors for Gamma-Ray Energies above 1 MeV”, Nuclear Science Symposium Conference Record (NSS/MIC), pp. 2012-2016, 2009.